

NASA Technical Memorandum 106213  
AIAA-93-0805

IN-20

159285

P.11

# Pulsed Laser Rayleigh Scattering Diagnostic for Hydrogen/Oxygen Rocket Exit Plane Flowfield Velocimetry

Frank J. Zupanc  
Lewis Research Center  
Cleveland, Ohio

Prepared for the  
31st Aerospace Sciences Meeting  
sponsored by the American Institute of Aeronautics and Astronautics  
Reno, Nevada, January 11-14, 1993



(NASA-TM- 106213 | PULSED LASER  
RAYLEIGH SCATTERING DIAGNOSTIC FOR  
HYDROGEN/OXYGEN ROCKET EXIT PLANE  
FLOWFIELD VELOCIMETRY (NASA) 11 p

N93-26149

Unclas

G3/20 0159285

1. The first part of the document is a list of the names of the people who were present at the meeting.

2. The second part of the document is a list of the topics that were discussed during the meeting.

3. The third part of the document is a list of the actions that were taken during the meeting.

4. The fourth part of the document is a list of the dates when the actions were completed.

5. The fifth part of the document is a list of the people who were responsible for completing the actions.

6. The sixth part of the document is a list of the people who were present at the meeting.

7. The seventh part of the document is a list of the topics that were discussed during the meeting.

8. The eighth part of the document is a list of the actions that were taken during the meeting.

9. The ninth part of the document is a list of the dates when the actions were completed.

10. The tenth part of the document is a list of the people who were responsible for completing the actions.

11. The eleventh part of the document is a list of the people who were present at the meeting.

12. The twelfth part of the document is a list of the topics that were discussed during the meeting.

13. The thirteenth part of the document is a list of the actions that were taken during the meeting.

14. The fourteenth part of the document is a list of the dates when the actions were completed.

15. The fifteenth part of the document is a list of the people who were responsible for completing the actions.

16. The sixteenth part of the document is a list of the people who were present at the meeting.

17. The seventeenth part of the document is a list of the topics that were discussed during the meeting.

18. The eighteenth part of the document is a list of the actions that were taken during the meeting.

19. The nineteenth part of the document is a list of the dates when the actions were completed.

## **ERRATA**

**NASA Technical Memorandum 106098**

**Frank J. Zupanc  
National Aeronautics and Space Administration  
Lewis Research Center  
Cleveland, Ohio 44135**

**The report number for the aforesaid Technical Memorandum is corrected to NASA Technical Memorandum 106213.**



# PULSED LASER RAYLEIGH SCATTERING DIAGNOSTIC FOR HYDROGEN/OXYGEN ROCKET EXIT PLANE FLOWFIELD VELOCIMETRY†

Frank J. Zupanc\*  
National Aeronautics and Space Administration  
Lewis Research Center  
Cleveland, OH 44135

## Abstract

A Doppler-resolved, pulsed laser Rayleigh scattering diagnostic has been developed to obtain local flowfield velocity measurements at the exit plane of a low thrust hydrogen/oxygen rocket engine operating in a high-altitude test facility. Fiberoptic signal collection was employed to obtain the forescatter and backscatter Doppler shifts necessary to resolve the axial and radial velocity components. A radial profile was obtained by traversing the collection probes along the beam path at the nozzle exit. The results are compared with theoretical predictions from a full Navier-Stokes model (RK/RPLUS). Significant discrepancies between the measured and predicted axial velocity profiles are observed, in terms of both magnitude and character. Radial velocity measurements exhibit excellent agreement with predictions near the centerline but show some departure off-axis. The discrepancies between theory and experiment are potentially the result of enhanced mixing between the core and fuel-film region beyond that predicted, and/or flow stratification between the hydrogen and oxygen injected into the central core region.

## Nomenclature

### English Symbols

$c$	speed of light
$\mathbf{C}$	random molecular velocity vector
$C_{\text{eff}}$	optical collection efficiency
$C_{\text{mp}}$	most probable molecular speed = $\sqrt{\frac{2kT}{m}}$
$d$	Fabry-Perot mirror spacing
$f(\nu - \nu_0)$	Rayleigh scattering frequency distribution function
$f_0$	peak position of unshifted laser profile (in bins)
$f_R$	peak position of shifted Rayleigh profile (in bins)
$F_i$	Fabry-Perot instrument finesse
$f_{\text{sr}}$	free spectral range calibration (in bins)
FSR	free spectral range = $\frac{c}{2nd}$
$I_T$	instrument intensity transmission
$k$	Boltzmann's constant
$\mathbf{k}_0$	incident laser wave vector
$\mathbf{k}_S$	scattered wave vector
$K$	scattering vector magnitude
$\mathbf{K}$	scattering wave vector = $\mathbf{k}_S - \mathbf{k}_0$
$m$	molecular mass
$n$	index of refraction
$N$	number density

$N_0$	number density at standard conditions
$P_0$	incident laser power
$P_B$	luminous background power
$P_R$	Rayleigh scattered power
$P_W$	stray scattered laser power
$r$	radial position on optical fiber exit face
$R$	radius of optical fiber core
$T$	gas temperature
$\mathbf{U}$	mean gas velocity vector
$\mathbf{V}$	total molecular velocity vector = $\mathbf{U} + \mathbf{C}$
$V_P$	probe volume
$Y(\nu)$	measured spectral profile

### Greek symbols

$\theta$	angle of incidence relative to Fabry-Perot mirror
$\theta_S$	scattering angle between $\mathbf{k}_0$ and $\mathbf{k}_S$
$\lambda$	wavelength
$\lambda_0$	incident laser wavelength
$\lambda_{\text{scattered}}$	scattered laser wavelength
$\nu$	frequency
$\nu_0$	incident laser frequency
$\Delta\nu$	net Doppler shift
$\Delta\nu_{\text{FWHM}}$	Rayleigh Doppler full-width at half-maximum
$\sigma$	Rayleigh scattering cross-section
$\Omega$	collection solid angle

### Subscripts

1	axial coordinate direction
2	radial coordinate direction
f	forescatter direction
b	backscatter direction

† Title differs from that in program abstract.

\* Aerospace Engineer, Member AIAA.

## Introduction

Low thrust chemical rocket engines are currently used in almost all spacecraft auxiliary propulsion systems (APS). Optimizing the performance of the APS is of critical importance as it directly impacts the spacecraft's payload and operational lifetime. Analytical approaches for chemical rocket performance optimization are employed to minimize expensive hardware testing and modifications. Performance models based on the JANNAF methodology<sup>1</sup>, however, are generally inadequate for low thrust chemical rockets with thick, reacting boundary layers.<sup>2</sup> Recent efforts have been directed toward the development of more rigorous predictive codes which are better suited to addressing the combustion and gas dynamic phenomena occurring inside smaller engines. These include the development of the VIPER code<sup>2</sup> in which the thin-boundary layer model used in the standard JANNAF approach has been replaced with a fully-viscous, 2-D parabolized Navier-Stokes model. More recent efforts include the development of the RPLUS<sup>3-5</sup> and LTPC<sup>6</sup> codes. These models extended the two-dimensional Navier-Stokes treatment into the combustor section, thus providing improved means for analyzing the reacting shear layers present in fuel-film cooled thrusters. Extensive experimental code validation at both the global and local levels is required, however, before they can be effectively utilized as optimization tools for designing small chemical rocket engines.

To provide localized data for code validation, a Doppler-resolved continuous wave (cw) laser Rayleigh scattering technique was previously developed at the NASA Lewis Research Center.<sup>7,8</sup> Velocity, temperature, and number density measurements were obtained in the low density, near-field plume region of a hydrogen/oxygen rocket engine. Measurements at the actual exit plane, however, could not be obtained due to luminous interferences emanating from the combustor and nozzle sections. These interferences were avoided by propagating the laser beam diagonally through the plume and orienting the collection optics to stare across the exit, as shown in Figure 1a. This arrangement results in the measurements being obtained at a significant distance downstream from the exit plane. In order to directly compare the measurements with theory, the flowfield predictions had to be extended into the near-field plume region, which introduced additional complexities into the analyses. In addition, restricted

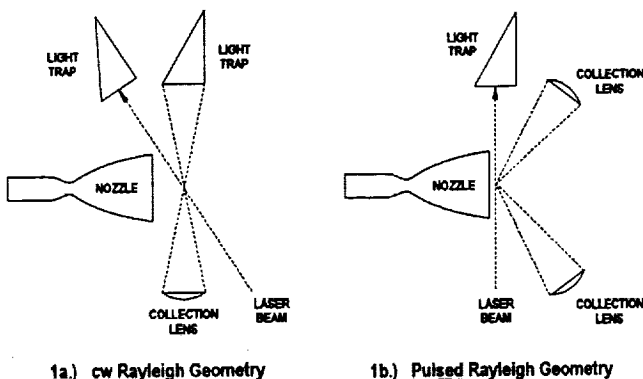
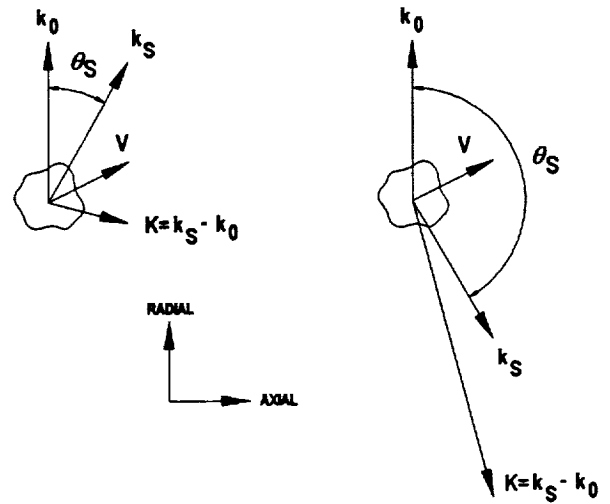


Figure 1. Comparison of cw and pulsed laser Rayleigh scattering optical arrangements near the exit plane of a hydrogen/oxygen rocket engine.



2a.) Forescatter

2b.) Backscatter

Figure 2. Scattering momentum transfer diagrams for forescatter ( $\theta_s=30^\circ$ ) and backscatter ( $\theta_s=150^\circ$ ) geometries shown relative to thruster axial and radial coordinate axes.

optical access inside the altitude test chamber made the diagonal passage of the laser beam difficult to implement on nozzles with large exit diameters. This limited the flexibility with which the cw technique could be applied to a range of different engine configurations.

This paper describes the modification of the cw laser Rayleigh diagnostic to utilize a high-energy, pulsed Nd:YAG laser. When used with time-gated signal detection, sensitivity to luminous background interferences could be greatly reduced without having to resort to the diagonal beam arrangement used for the cw measurements. The pulsed laser beam could be passed parallel to the nozzle exit with the collection optics staring into the nozzle, as shown in Figure 1b. This enabled direct comparison of the measured data with predictions at the actual exit plane, thereby simplifying the analyses. In addition, the flexibility with which the technique could be applied to nozzles where the optical access was more restricted could be significantly improved.

## Theoretical Background

A more extensive description of the Rayleigh scattering theory is given in References 7 and 8. Only a brief description will be repeated here. The following discussion is limited to scattering from a sufficiently rarefied medium for which Brillouin scattering can be neglected. The scattering momentum transfer diagrams for the two geometries used in this investigation are shown in Figure 2. The Doppler shift in the frequency of Rayleigh scattered light from a molecule moving with total velocity vector  $\mathbf{V}$  is given by the following expression:

$$\nu - \nu_0 = \frac{1}{2\pi} \mathbf{K} \cdot \mathbf{V} \quad (1)$$

Assuming that the random molecular velocity component follows a Maxwellian velocity distribution function, the Rayleigh scattering frequency distribution function for a given species  $i$  can be expressed as:

$$f_i(\nu - \nu_0) \cdot d\nu = \frac{2\sqrt{\pi}}{C_{mp,i} K} \exp \left[ - \left( \frac{2\pi(\nu - \nu_0) - \mathbf{K} \cdot \mathbf{U}}{C_{mp,i} K} \right)^2 \right] \cdot d\nu \quad (2)$$

The Rayleigh spectrum for species  $i$  is a Gaussian-shaped profile whose full-width at half-maximum (FWHM) is given by the following expression:

$$\Delta \nu_{FWHM,i} = 0.265 \cdot C_{mp,i} K \quad (3)$$

Thus the width of the Rayleigh profile is proportional to the square root of the ratio of the translational temperature to the molecular mass of the species. The net Doppler shift in the peak of the Rayleigh profile is then related to the mean gas velocity  $\mathbf{U}$  through the following expression:

$$\nu - \nu_0 = \frac{1}{2\pi} \mathbf{K} \cdot \mathbf{U} \quad (4)$$

The Rayleigh scattered power into frequency interval  $d\nu$  for a multispecies gas mixture can then be expressed as:

$$P_R(\nu - \nu_0) \cdot d\nu = C_{eff} P_0 V_P \Omega \sum_i N_i \left( \frac{d\sigma}{d\Omega} \right)_i f_i(\nu - \nu_0) \cdot d\nu \quad (5)$$

For linearly polarized incident light, the Rayleigh differential scattering cross-section at  $90^\circ$  relative to the electric polarization vector is given by the following expression:<sup>9</sup>

$$\left( \frac{d\sigma}{d\Omega} \right)_i = \frac{4\pi^2 (n_i - 1)^2}{N_0^2 \lambda_0^4} \quad (6)$$

Thus the resultant Rayleigh spectrum is the number density and differential scattering cross-section weighted sum contribution of each species in the mixture. Differential cross-sections for the species relevant to this investigation are calculated using gas refractivity data in Reference 10 and are listed in Table 1.

If the gas consists of a single component, or the composition is known, then analysis of the Rayleigh scattering spectra can simultaneously yield the translational temperature, total number density, and the mean gas velocity. If the composition is unknown, determination of the temperature and number density are considerably more difficult, if not impossible. During the previous applications of the cw Rayleigh diagnostic in References 7 and 8, it was shown that for a fuel-

**Table 1. Calculated Rayleigh scattering differential cross-sections for relevant species at  $\lambda_0 = 532$  nm (based on refractivity data in Reference 10).**

Species	Molecular Weight	$\left( \frac{d\sigma}{d\Omega} \right) \times 10^{-32} \text{ (m}^2/\text{steradian)}$
H	1	0.932
H <sub>2</sub>	2	1.331
H <sub>2</sub> O	18	4.374
N <sub>2</sub>	28	6.147
O	16	1.080
OH	17	9.364
O <sub>2</sub>	32	5.067

rich condition consisting primarily of water with excess hydrogen, temperature and water number density estimates could be obtained by assuming that the mixture consisted only of water. The errors associated with neglecting the presence of even large mole fractions of hydrogen were relatively small. This was due to the fact that the scattering was almost entirely dominated by the larger water molecules. The oxidizer-rich condition, however, was the opposite as both oxygen and water contributed almost equally. Their different molecular weights made determination of the temperature difficult if the relative number densities of the two species were not known in advance.

In the previous studies<sup>7,8</sup>, a thruster was employed which utilized only a small amount of fuel-film cooling (15%). This resulted in a core zone which was nearly stoichiometric or slightly fuel-rich. For an engine with relatively high combustion efficiency, most of the oxygen would have been consumed. Temperature and number density could then be estimated by assuming that water was the dominant scattering species in the exhaust. The presence of varying amounts of unreacted hydrogen was not important in this analyses. In the current investigation, the assumption that an overall fuel-rich condition exists throughout the thruster flowfield could no longer be made. This is due to the relatively large percentage of fuel-film cooling (75%) employed in the thruster used in this investigation. This resulted in a highly oxidizer-rich core flow which transitions to a highly fuel-rich boundary layer at the nozzle wall. Thus temperature and number density estimates were not obtained for this investigation as knowledge of the species composition was not known or measured. The emphasis in this investigation was then placed on the measurement of the mean gas velocity as estimated from the net Doppler shifts in the Rayleigh scattering spectral profiles. This was possible since the net Doppler shift is a function only of the scattering geometry and the mean velocity, and is essentially independent of the species composition.

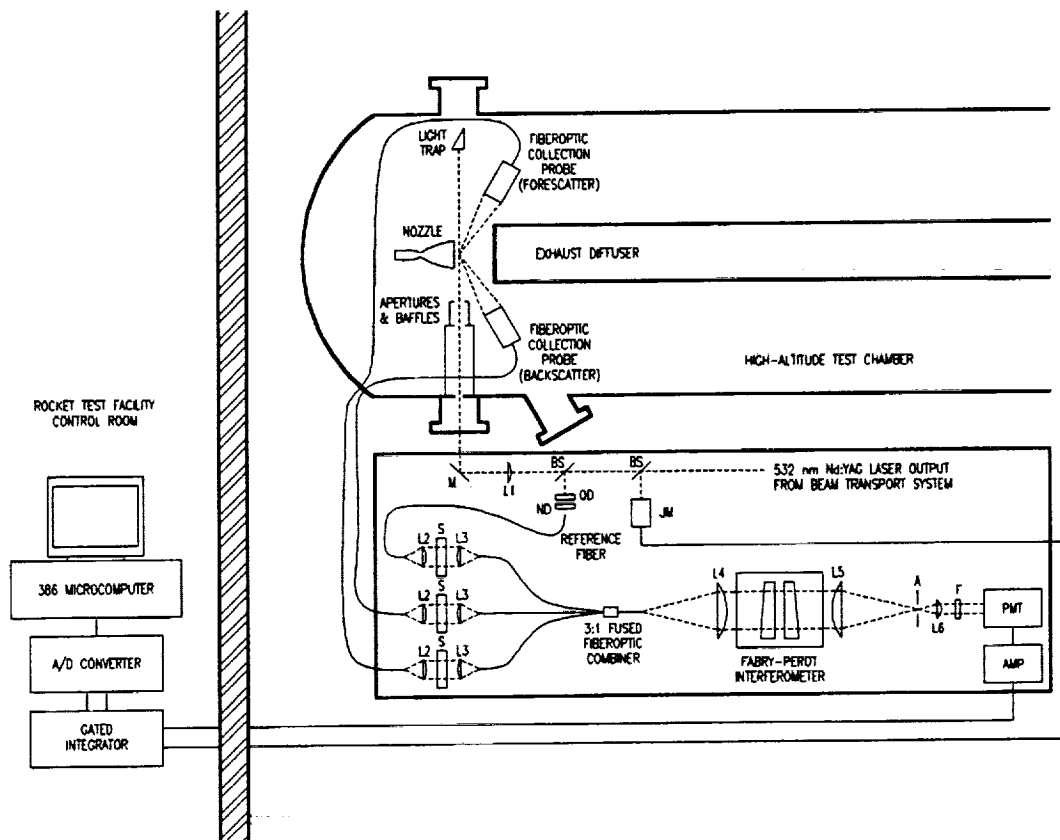


Figure 3. Schematic diagram of overall optical arrangement for pulsed Rayleigh scattering diagnostic.

## Experimental Approach

### Thruster and Test Facility

The Rayleigh scattering diagnostic was implemented in a low thrust rocket test facility at the NASA Lewis Research Center. The facility was developed to support performance and life testing of gaseous hydrogen/oxygen rocket engines with thrust levels of 22-220 N. Thruster testing was conducted in a low pressure test chamber capable of simulating an altitude of 35 km. The altitude chamber measured 1.82 m in length by 0.91 m in diameter. Three optical access ports were located at 90° relative to the thruster axis with a fourth additional port canted at a 60° angle relative to the thruster axis. A complete description of this facility is given in Reference 11. A supersonic diffuser with a diameter of 102 mm was used to capture the rocket exhaust and transport it outside of the test chamber. The diffuser was located an axial distance of approximately 80 mm downstream from the thruster exit plane. The general placement of the nozzle and diffuser within the test chamber are shown schematically in Figures 3 and 4 along with the Rayleigh diagnostic system. The back pressure in the tank was approximately 1.2 kPa and remained relatively constant during the course of the testing.

A gaseous hydrogen/gaseous oxygen 110 N thrust rocket engine developed by the GenCorp Aerojet Propulsion Division in support of the auxiliary propulsion system for Space Station Freedom was used in this investigation. A complete description

of the thruster specifications is given in Reference 12. A simplified schematic of the thruster flowfield is shown in Figure 5. The thruster was operated at a chamber pressure of approximately 496 kPa with 75% of the hydrogen injected along the wall as a film coolant. The nozzle exit area ratio was 33:1 with an exit diameter of 73.8 mm. The remainder of the hydrogen and all of the oxygen was injected into the core region and ignited with a spark plug. Prior to injection, the hydrogen was passed through coolant channels in the nozzle wall to regeneratively cool the chamber. The overall mixture ratio

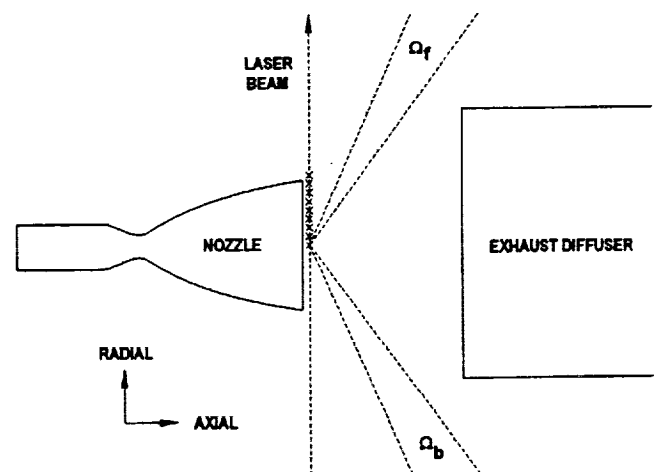


Figure 4. Schematic diagram showing relative positions of nozzle, diffuser, laser beam, forscatter and backscatter collection solid angles, and measurement locations.



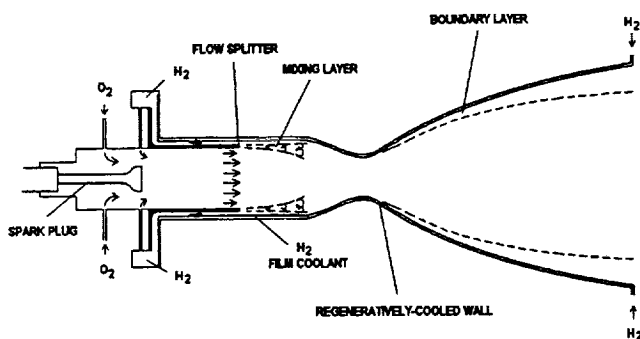


Figure 5. Schematic diagram of thruster geometry.

(M.R.) was approximately 5.0, which yielded a highly oxidizer-rich core M.R. of 20. This was expected to result in strong variation in local M.R. at the nozzle exit from the highly oxidizer-rich region near the centerline to the highly fuel-rich region in the film coolant zone at the nozzle wall. This wide range of uncertainty in the local gas composition prohibited the unambiguous estimation of temperature and number density from the Rayleigh scattering measurements. Mean gas velocity estimates, however, could still be obtained from the Rayleigh scattering profiles, as these were insensitive to variations in gas composition.

### Diagnostic Instrumentation

The pulsed Rayleigh system utilized the second harmonic output from an injection-seeded Nd:YAG laser (532 nm, 800 mJ/pulse, 10 Hz pulse rate, 8 ns pulse duration, ~ 150 MHz spectral bandwidth). The beam was transported by a system of relay mirrors from an environmentally-controlled laser room into the low thrust rocket test facility. As shown in Figure 3, a beam splitter (BS) was used to reflect part of the incident beam (<0.25%) into a Joule meter (JM) for measurement of the pulse energy. A second identical beam splitter was used to direct some of the laser light onto a ground quartz diffuser (QD), through a stack of neutral density filters (ND), and into a 1000 micron diameter optical fiber. This reference signal was used to measure the unshifted laser peak position and to evaluate the Fabry-Perot instrument response function. The primary beam was then passed through a 1 m focal length lens and reflected with a mirror (M) through the tank window and parallel to the nozzle exit inside the altitude test chamber. The incident laser beam was vertically polarized relative to the optical plane, thereby maximizing the polarization-dependent Rayleigh scattering signal. A set of apertures and baffles were used to minimize stray light scattered within the chamber. A light trap was used to terminate the beam inside the tank.

Two identical fiberoptic signal collection probes were used to obtain the forescatter and backscatter spectral profiles. The separate forescatter and backscatter measurements were needed to resolve both the axial and radial velocity components, since the Doppler shift in either direction was a function of both velocity components. This is evident in the momentum transfer diagrams in Figure 2. Physical restrictions within the altitude test chamber did not permit the orientation of the scattering geometry in a manner that the Doppler shift for a given direction was a function of only one velocity component. The scattering

angles for the forescatter and backscatter geometry's were approximately 30° and 150°, respectively. The intersection of the collection probe optical path with the incident laser beam yielded a spatial sampling extent in the radial direction of approximately 3 mm. The scattered light was then transported via two 1000 micron diameter fiber optic cables outside of the altitude chamber and lens-coupled (using L2 and L3), along with a laser line reference fiber, into a fused 3:1 fiberoptic combiner. Input to the combiner was controlled using electromechanical shutters (S), thus allowing rapid selection between the forescatter, backscatter, or reference input signals.

The single leg output of the fiberoptic combiner was then collimated using an achromatic doublet (L4) through a microcomputer-controlled, scanning Fabry-Perot interferometer (70 mm clear aperture, 21.4 GHz free spectral range). The transmitted light was then focused (L5) through an aperture (A) and recollimated (L6) through a narrowband, dielectric interference filter (F) ( $\lambda=532$  nm, 10 nm bandwidth, 50% minimum peak transmission) to reject light outside of the spectral region of interest. The transmitted light was then measured with a thermoelectrically-cooled, gallium arsenide photomultiplier tube (PMT) operated at a current gain of approximately  $1 \times 10^6$ . The specified quantum efficiency of the photocathode at 532 nm was approximately 20%. The PMT output was then amplified with a low noise preamplifier (1 GHz bandwidth, 32.5 dB gain) and then input to a time-gated voltage integrator. A 100 ns gate width was found to provide an adequate rejection of the continuous background while providing easy synchronization with the 8 ns laser pulse. The gated integrator output was then digitized and stored in a microcomputer for later analysis. The output from the Joule meter was also digitized and stored to correct for pulse-to-pulse fluctuations in laser energy.

The finite diameter of the laser beam, combined with the need to reduce light spuriously scattered from the nozzle, forced the measurements to be obtained at an axial distance of approximately 3 mm downstream of the actual exit plane. This distance was much smaller than the nozzle radius of 36.9 mm. Analyses using the Standardized Plume Flowfield (SPF-II)<sup>13</sup> model have shown that the flowfield properties at this downstream distance show negligible departure from those at the thruster exit plane, except in the small outermost region at the plume boundary. Thus, the measurements obtained at this axial position can effectively be considered to be those taken at the exit plane. In contrast, several of the *cw* Rayleigh scattering measurements were obtained at an axial distance that was over one nozzle radius downstream of the exit plane.<sup>7,8</sup> SPF-II plume analysis showed that the departure in the flowfield properties at these positions from those at the exit plane was no longer negligible. Thus the plume expansion effects had to be considered over the entire radial profile for the *cw* measurements. With the pulsed measurement, however, these effects are confined to only the outermost radial positions and do not significantly affect the interior measurements.

### Experimental Procedure

Steady state run duration's in the altitude facility were generally limited to 30 seconds per test. This limit was caused by the accumulation of hydrogen inside the altitude chamber due to incomplete capture of the exhaust plume by the diffuser. Due

to the restricted run duration, foreshatter and backscatter measurements were acquired on separate runs. Each foreshatter and backscatter measurement at each radial position was typically repeated three to five times in order to assess experimental repeatability. The process for acquiring foreshatter and backscatter measurements was identical. Before the engine was fired, the reference shutter was opened and a reference measurement of the unshifted laser line was obtained. This measurement would subsequently be used to obtain the instrument response function of the Fabry-Perot interferometer. For the pulsed measurements, the piezoelectric spacer elements in the Fabry-Perot were scanned in a stepped-ramp mode. The voltage at each ramp position was fixed while a given number of samples from the gated integrator were digitized and stored in a microcomputer system. The ramp voltage was then increased to the next position and the sampling procedure was repeated. This process was repeated until the scan covered two adjacent interference orders. Typically, fifty ramp intervals, or bins, were used for the reference scans, with ten samples per bin being acquired.

Following acquisition of the reference spectra, the engine was ignited and the Rayleigh scattering measurements from the exhaust were obtained. This process was nearly identical to the acquisition of the reference spectra except that the scan contained only half as many bins. This was done in order to maximize the number of samples per bin for the limited run duration in order to increase the signal-to-noise ratio. Typically, the Rayleigh spectra contained 25 bins with ten samples per bin. Radial profiles across the nozzle exit were obtained by traversing the foreshatter and backscatter fiberoptic collection probes along the beam path using electromechanical translation stages. The measurement positions relative to the nozzle exit used in this investigation, along the collection solid angles of the fiberoptic probes, are shown in Figure 4.

### Data Analyses

The analyses of the Rayleigh scattering measurements were essentially the same as that described in References 7 and 8. The maximum likelihood curve fitting procedure described in Reference 14 was used to fit the reference and Rayleigh model functions to the experimental data. The instrument function was modeled by spatially integrating the Airy intensity transmission coefficient over the finite exit area of the fiberoptic combiner, which is given by the following expression:

$$I_T(\nu) = \int_0^R \frac{2dr}{r \left[ 1 + \frac{4F_1}{\pi^2} \sin^2 \left( \frac{2\pi r m d \cos \theta}{c} \right) \right]} \quad (7)$$

The angle of incidence with respect to the Fabry-Perot is related to the radial position  $r$  on the fiberoptic combiner's exit face through the following expression:

$$\theta = \tan^{-1} \left( \frac{r}{\text{focal length}_{L4}} \right) \quad (8)$$

The  $L4$  subscript refers to the focal length of the Fabry-Perot collimating lens in Figure 3. Parameters estimated for the reference spectra included the unshifted laser peak position, the free spectral range calibration, and the total etalon finesse. Data from a typical reference scan along with the associated curve fit are shown in Figure 6a.

The Rayleigh profiles measured during the engine firings actually represent the convolution of the Fabry-Perot instrument function given in expression 7 with the various source spectra, including that from Rayleigh scattering, stray light scattering, and background luminosity. This convolution can be expressed as:<sup>15-17</sup>

$$Y(\nu) = \int_{-\infty}^{\infty} [P_R(\nu') + P_W(\nu') + P_B] \cdot I_T(\nu - \nu') \cdot d\nu' \quad (9)$$

The maximum likelihood curve fitting procedure in Reference 14 was then used to fit the model function in expression 9 to the measurements obtained during the engine firing. Estimated parameters included the Rayleigh scattered power, the stray light scattered power, the luminous background power, the half-width of the Rayleigh profile, and the central peak position in the Rayleigh profile. Representative hot fire data along with the associated maximum likelihood curve fit are shown in Figure 6b. The horizontal scales for the reference and hot fire measurements in Figures 6a and 6b are the same. The broadening and net shift in the Rayleigh peak in the hot fire measurement is clearly evident relative to the unshifted line profile in the reference measurement. Interferences from unshifted, stray light are minimal in this example.

The net Doppler shifts in the foreshatter and backscatter directions were then used to estimate the axial and radial velocities for a given radial position using the following expressions:

$$K_{f1}U_1 + K_{f2}U_2 = \Delta\nu_f \quad (10)$$

$$K_{b1}U_1 + K_{b2}U_2 = \Delta\nu_b \quad (11)$$

### Error Analyses

The curve fitting procedure yields both the mean and standard error estimates for the fitted parameters. The error estimates from the curve fits are associated with the random errors in the measurements. These are primarily associated with random shot noise due to photon statistics, electrical noise in the signal amplification process, and vibrations induced into the interferometer by acoustic disturbances within the test cell. The curve fit parameters whose errors significantly affect the velocity estimates include the unshifted laser peak position, the free spectral range calibration, and the shifted Rayleigh peak position. Other sources of error include bias terms associated with uncertainty in the Fabry-Perot mirror spacing and the scattering angles for the foreshatter and backscatter geometries. Additional errors are associated with drift in the Fabry-Perot alignment and instability in the laser frequency during the course of a single scan. As a new reference measurement is

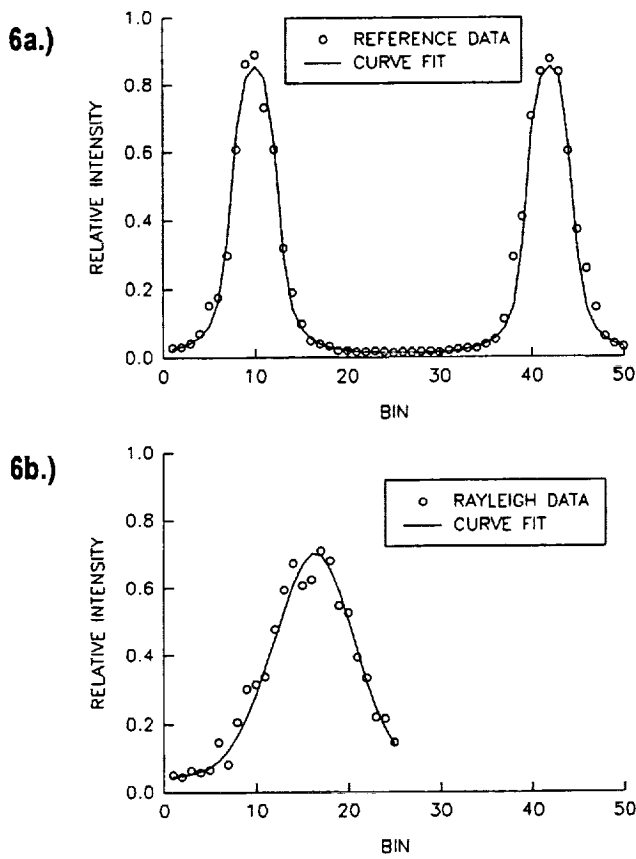


Figure 6. Typical Fabry-Perot scan measurements for reference line (top) and backscatter Rayleigh measurement in rocket exhaust (bottom).

acquired for each hot fire measurement, long-term drift is not considered a problem.

For the sources of bias errors, uncertainty in the mirror spacing is most significant, as this directly affects knowledge of the absolute free spectral range (FSR) of the interferometer. The standard error in the mirror spacing is estimated to be 0.17 mm, which corresponds to an uncertainty in the free spectral range of 520 MHz. Uncertainty in the scattering angles are less than 2%, which tends to have a negligible effect on the velocity estimates relative to the other sources of uncertainty. Errors due to drift in the Fabry-Perot alignment and the laser frequency would manifest themselves in the estimates of the unshifted peak position and free spectral range calibrations in the reference measurements. Since run to run variations in the mean values for these parameters were typically much less than the standard error estimates for these parameters, these effects were not considered significant.

The net Doppler shift using the fitted parameters can be expressed as:

$$\Delta\nu = (f_R - f_0) \cdot \left[ \frac{\text{FSR}}{f_{sr}} \right] \quad (12)$$

The total standard error estimate for the net Doppler shifts can then be obtained by applying the error propagation equation<sup>18</sup> to expression 12 which yields the following expression (note that the  $\sigma$  terms symbolize the standard deviation, not the scattering cross-section):

$$\sigma_{\Delta\nu}^2 = (\sigma_{f_R}^2 + \sigma_{f_0}^2) \cdot \left( \frac{\text{FSR}}{f_{sr}} \right)^2 + \sigma_{\text{FSR}}^2 \cdot \left( \frac{f_R - f_0}{f_{sr}} \right)^2 + \sigma_{f_{sr}}^2 \cdot \left( -(f_R - f_0) \cdot \left( \frac{\text{FSR}}{f_{sr}^2} \right) \right)^2 \quad (13)$$

The standard error estimates for the axial and radial velocities are obtained by explicitly solving expressions 10 and 11 for  $U_1$  and  $U_2$  and applying the error propagation analysis, which yields the following expressions:

$$\sigma_{U_1}^2 = \sigma_{\Delta\nu}^2 \cdot \left( \frac{2\pi}{K_{f1} - \frac{K_{f2}K_{b1}}{K_{b2}}} \right)^2 + \sigma_{\Delta\nu_b}^2 \cdot \left( \frac{-2\pi K_{f2}}{K_{f1}K_{b2} - K_{f2}K_{b1}} \right)^2 \quad (14)$$

$$\sigma_{U_2}^2 = \sigma_{U_1}^2 \cdot \left( -\frac{K_{b1}}{K_{b2}} \right)^2 + \sigma_{\Delta\nu_b}^2 \cdot \left( \frac{2\pi}{K_{b2}} \right)^2 \quad (15)$$

This analysis assumes that the various error terms are uncorrelated. This is generally the case where stray light scattered interferences are small. In situations where these interferences are significant, the individual uncertainties will exhibit varying degrees of interdependency, and should be considered in the error propagation analysis. Fortunately, stray light interferences were minimized to the extent that the correlation terms were not considered necessary.

## Results

Preliminary results for the axial and radial velocities are shown in Figures 7 and 8, respectively, along with nozzle exit plane flowfield predictions obtained using the RK/RPLUS code.<sup>5</sup> The vertical error bars represent the combined uncertainties from the individual curve fit parameters and the Fabry-Perot mirror spacing. The horizontal error bars represent the spatial sampling extent of the probe volume which is approximately 3 mm in the radial direction. The actual uncertainty in the center position of the probe volume is on the order of 500 microns.

The axial velocity estimates show considerable departure in both magnitude and character from the RK/RPLUS predictions. The predicted profile is relatively flat in the core region and

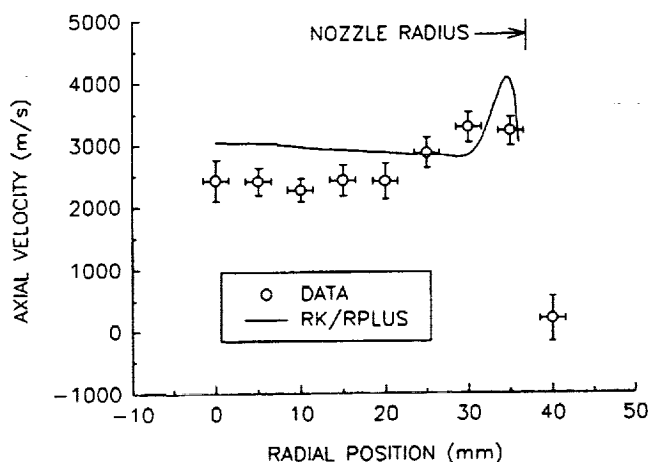


**Figure 7. Comparison of axial velocity measurements with RK/RPLUS predictions. Vertical error bars represent total standard error estimates ( $1-\sigma$ ), while horizontal bars represent spatial sampling extent.**

increases sharply in the fuel-film layer. This is due to the increased acceleration experienced by the lighter hydrogen film than by the heavier oxidizer-rich core gases. The discrepancies between the measured and predicted profiles may be due to increased core/film mixing beyond that predicted by the RK/RPLUS code. This increased mixing would manifest itself in a velocity profile which increases more gradually with radial position, as is shown in the data in Figure 7. This is in contrast with the steep velocity gradient between the core and film regions evident in the RK/RPLUS prediction. The error associated with the predicted mixing of the core and film regions may be caused by the manner in which the injection of the film is modeled. It is assumed that the sleeve which separates the film from the core flow is infinitely thin and therefore would produce negligible recirculation effects. The actual finite thickness of the sleeve, however, may cause the formation of a recirculation zone which in turn acts to enhance the turbulent mixing between the two flow regions.

The another potential source of disagreement may be flow stratification within the oxidizer-rich core flow. The RK/RPLUS analyses assumes a well-mixed, fully-reacted core flow. The emphasis is placed on modeling the core/film interaction. It is possible, however, that the oxygen and hydrogen within the core are not completely mixed. Instead, they themselves form a reacting shear layer which propagates from the injector core into the combustion chamber and through the nozzle. This hypothesis is based on Raman scattering measurements of oxygen number density made using the same injector and chamber configuration, but with the nozzle cut off at an area ratio of approximately 1.4.<sup>19</sup> These measurements show a considerably higher oxygen number density near the centerline than is predicted by the RK/RPLUS model. This central zone of heavy, unreacted oxygen would tend to be accelerated to a lesser extent than the lighter products of a fully-reacted mixture. This, combined with the energy release losses associated with flow stratification, may account for the lower than predicted velocity measurements. Further measurements are required, however, before either the increased core/film mixing or core flow stratification effects can be verified.

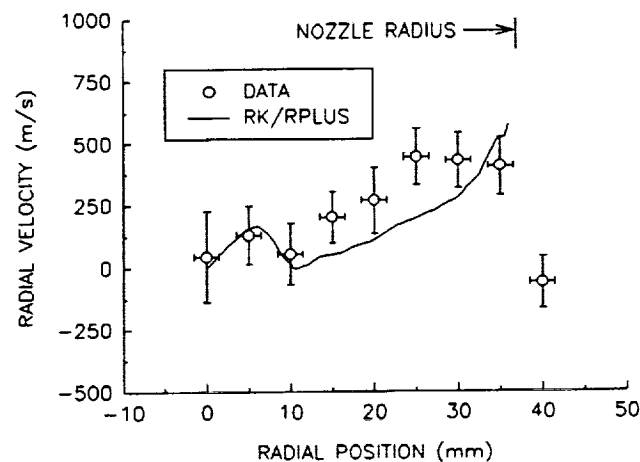


**Figure 8. Comparison of radial velocity measurements with RK/RPLUS predictions. Vertical error bars represent total standard error estimates ( $1-\sigma$ ), while horizontal bars represent spatial sampling extent.**

The radial velocity profile shows generally good agreement with the RK/RPLUS predictions, particularly near the centerline of the nozzle. There seems to be some disagreement in magnitude between the data and theory with increasing radial position, but these discrepancies tend to fall close to the limits of experimental accuracy. The generally good agreement, however, seems to indicate that the flow divergence within the nozzle is adequately modeled.

## **Concluding Remarks**

A Doppler-resolved, pulsed laser Rayleigh scattering diagnostic utilizing fiberoptic signal collection was successfully applied to obtain flowfield velocimetry measurements at the exit plane of a low thrust, hydrogen/oxygen rocket engine. The utilization of a pulsed Nd:YAG laser with time-gated signal detection eliminated interferences from background luminosity emanating from the combustion chamber. These interferences previously prevented the application of *cw* Rayleigh diagnostic at the exit. The axial and radial velocity measurements at the exit show considerable departure from predictions obtained using a full Navier-Stokes RK/RPLUS model. These discrepancies are believed to be due to increased shear layer interaction between the core/film regions beyond that predicted, and/or flow stratification within the core region itself due to incomplete mixing of the hydrogen and oxygen. Further measurements should be obtained, particularly near the injector using a species sensitive technique, such as laser Raman scattering, in order to more definitively characterize these effects.

## **Acknowledgments**

The author would like Jonathan M. Weiss for his assistance in providing the RK/RPLUS predictions and useful discussions concerning the comparison of the results. The author would also like to thank Lynn Arrington for her patience and dedication in operating the rocket test facility during the course of these experiments.

## References

1. "JANNAF Rocket Engine Performance Prediction and Evaluation Manual," CPIA Pub. 246, 1975.
2. Berker, D.R., Coats, D.E., Dang, A.L., Dunn, S.S., and Kehtarnavaz, H., "Viscous Interaction Performance Evaluation Routine for Nozzle Flows with Finite Rate Kinetic Chemistry (VIPER)," AL-TR-90-042, 1990.
3. Weiss, J.M. and Merkle, C.L., "Numerical Investigation of Reacting Flowfields in Low-Thrust Rocket Engine Combustors," AIAA-91-2080, 1991.
4. Weiss, J.M., Daines, R.L., and Merkle, C.L., "Computation of Reacting Flowfields in Low-Thrust Rocket Engines," AIAA-91-3557, 1991.
5. Weiss, J.M. and Merkle, C.L., "Prediction of Engine and Near-Field Plume Reacting Flows in a Low-Thrust Chemical Rocket," AIAA-93-0237, 1993.
6. Dang, A., Navaz, H.K., and Gross, K.W., "Solution of Two-Phase Reacting Flow in Liquid Thrust Chambers," 28th JANNAF Combustion Subcommittee Meeting, Brooks AFB, San Antonio, TX, 1991.
7. Seasholtz, R.G., Zupanc, F.J., and Schneider, S.J., "Spectrally Resolved Rayleigh Scattering Diagnostic for Hydrogen-Oxygen Rocket Plume Studies," *Journal of Propulsion and Power*, **8**, 935-942, 1992.
8. Zupanc, F.J. and Weiss, J.M., "Rocket Plume Flowfield Characterization Using Laser Rayleigh Scattering," AIAA-92-3351, 1992.
9. Penney, C.M., "Light Scattering in Terms of Oscillator Strengths and Refractive Indices," *Journal of the Optical Society of America*, **59**, 34-42, 1969.
10. Gardiner, Jr., W.C., Hidaka, Y., and Tanzawa, T., "Refractivity of Combustion Gases," *Combustion and Flame*, **40**, 213-219, 1981.
11. Arrington, L.A. and Schneider, S.J., "Low Thrust Rocket Test Facility," AIAA-90-2503, 1990.
12. Robinson, P.J., "Space Station Auxiliary Thrust Chamber Technology," NASA Contractor Report 185296, 1990.
13. Dash, S.M., Pergament, H.S., Wolf, D.E., Sinha, N., Taylor, M.W., and Vaughn, Jr., M.E., "The JANNAF Standardized Plume Flowfield Code Version II (SPF-II)," CR-RD-SS-90-4, 1990.
14. Press, W.H., Flannery, B.P., Teukolsky, S.A., and Vetterling, W.T., Numerical Recipes, Cambridge University Press, New York, NY, 1989.
15. Hernandez, G., Fabry-Perot Interferometers, Cambridge University Press, New York, NY, 1986.
16. Vaughan, J.M., The Fabry-Perot Interferometer: History, Theory, Practice, and Applications, IOP Publishing Ltd., Bristol, England, 1989.
17. Wilksch, P.A., "Instrument Function of the Fabry-Perot Interferometer," *Applied Optics*, **24**, 1502-1511, 1985.
18. Bevington, P.R. and Robinson, D.K., Data Reduction and Error Analysis for the Physical Sciences, McGraw-Hill, Inc., New York, NY, 1992.
19. de Groot, W.A. and Weiss, J.M., "Species and Temperature Measurement in  $H_2/O_2$  Rocket Flow Fields by Means of Raman Scattering Diagnostics," AIAA-92-3353, 1992.

REPORT DOCUMENTATION PAGE			Form Approved OMB No. 0704-0188	
Public reporting burden for this collection of information is estimated to average 1 hour per response, including the time for reviewing instructions, searching existing data sources, gathering and maintaining the data needed, and completing and reviewing the collection of information. Send comments regarding this burden estimate or any other aspect of this collection of information, including suggestions for reducing this burden, to Washington Headquarters Services, Directorate for Information Operations and Reports, 1215 Jefferson Davis Highway, Suite 1204, Arlington, VA 22202-4302, and to the Office of Management and Budget, Paperwork Reduction Project (0704-0188), Washington, DC 20503.				
1. AGENCY USE ONLY (Leave blank)		2. REPORT DATE January 1993		3. REPORT TYPE AND DATES COVERED Technical Memorandum
4. TITLE AND SUBTITLE  Pulsed Laser Rayleigh Scattering Diagnostic for Hydrogen/Oxygen Rocket Exit Plane Flowfield Velocimetry			5. FUNDING NUMBERS  WU-506-42-31	
6. AUTHOR(S)  Frank J. Zupanc				
7. PERFORMING ORGANIZATION NAME(S) AND ADDRESS(ES)  National Aeronautics and Space Administration Lewis Research Center Cleveland, Ohio 44135-3191			8. PERFORMING ORGANIZATION REPORT NUMBER  E-7739	
9. SPONSORING/MONITORING AGENCY NAMES(S) AND ADDRESS(ES)  National Aeronautics and Space Administration Washington, D.C. 20546-0001			10. SPONSORING/MONITORING AGENCY REPORT NUMBER  NASA TM- 106213 AIAA-93-0805	
11. SUPPLEMENTARY NOTES Prepared for the 31st Aerospace Sciences Meeting sponsored by the American Institute of Aeronautics and Astronautics, Reno, Nevada, January 11-14, 1993. Responsible person, Frank J. Zupanc, NASA Lewis Research Center, (216) 977-7483.				
12a. DISTRIBUTION/AVAILABILITY STATEMENT  Unclassified - Unlimited Subject Categories 20, 35, and 74			12b. DISTRIBUTION CODE	
13. ABSTRACT (Maximum 200 words)  A Doppler-resolved, pulsed laser Rayleigh scattering diagnostic has been developed to obtain local flowfield velocity measurements at the exit plane of a low thrust hydrogen/oxygen rocket engine operating in a high-altitude test facility. Fiberoptic signal collection was employed to obtain the forescatter and backscatter Doppler shifts necessary to resolve the axial and radial velocity components. A radial profile was obtained by traversing the collection probes along the beam path at the nozzle exit. The results are compared with theoretical predictions from a full Navier-Stokes model (RK/RPLUS). Significant discrepancies between the measured and predicted axial velocity profiles are observed, in terms of both magnitude and character. Radial velocity measurements exhibit excellent agreement with predictions near the centerline but show some departure off-axis. The discrepancies between theory and experiment are potentially the result of enhanced mixing between the core and fuel-film region beyond that predicted, and/or flow stratification between the hydrogen and oxygen injected into the central core region.				
14. SUBJECT TERMS  Laser Rayleigh scattering; Velocimetry; Auxiliary rocket propulsion			15. NUMBER OF PAGES 10	
			16. PRICE CODE A02	
17. SECURITY CLASSIFICATION OF REPORT Unclassified	18. SECURITY CLASSIFICATION OF THIS PAGE Unclassified	19. SECURITY CLASSIFICATION OF ABSTRACT Unclassified	20. LIMITATION OF ABSTRACT	